

TRANSPARENT BOUNDARY CONDITIONS BASED ON THE POLE CONDITION FOR TIME-DEPENDENT, TWO-DIMENSIONAL PROBLEMS

DANIEL RUPRECHT*, ACHIM SCHÄDLE†, AND FRANK SCHMIDT‡

Abstract. The pole condition approach for deriving transparent boundary conditions is extended to the time-dependent, two-dimensional case. Non-physical modes of the solution are identified by the position of poles of the solution's spatial Laplace transform in the complex plane. By requiring the Laplace transform to be analytic on some problem dependent complex half-plane, these modes can be suppressed. The resulting algorithm computes a finite number of coefficients of a series expansion of the Laplace transform, thereby providing an approximation to the exact boundary condition. The resulting error decays super-algebraically with the number of coefficients, so relatively few additional degrees of freedom are sufficient to reduce the error to the level of the discretization error in the interior of the computational domain. The approach shows good results for the Schrödinger and the drift-diffusion equation but, in contrast to the one-dimensional case, exhibits instabilities for the wave and Klein-Gordon equation. Numerical examples are shown that demonstrate the good performance in the former and the instabilities in the latter case.

Key words. transparent boundary condition, non-reflecting boundary condition, pole condition, wave equation, Klein Gordon equation, Schrödinger equation, drift diffusion equation

1. Introduction. Transparent boundary conditions (TBCs) are required whenever a problem is posed on a domain that has to be truncated in order to become numerically treatable, either because it is unbounded or too large to compute solutions in a reasonable amount of time. Usually, TBCs have to avoid reflections at the artificial boundary, although more complex situations can arise, for example if inhomogeneities are present in the truncated part. Exact TBCs are typically non-local in time and space and suitable approximations have to be derived in order to be able to efficiently compute numerical solutions to the truncated problem. The study of this type of boundary conditions started in the 1970s, see the paper of E. L. Lindman [15] and references given there. In their seminal paper [5] Engquist and Majda devised a general strategy for the derivation of approximate TBCs. Comprehensive overviews of the subject can be found, for example, in [2, 7, 8, 9, 23].

The pole condition approach for the derivation of TBCs was introduced in a first version in [20, 22] for time-dependent Schrödinger-type equations, later in [12, 13, 19] for time-harmonic scattering problems. It was further explored in [6, 11, 16, 21]. An alternative formulation of the pole condition is presented in [17], which provides a noticeably simplified implementation and is also used in the present paper. A comparison of different techniques to derive TBCs for Schrödinger's equation can be found in [2], finding the pole condition to be one of the most efficient. In [18], the pole condition approach is adopted for a larger class of time-dependent problems, showing good performance for different types of partial differential equations (PDEs) ranging from Schrödinger's equation, the heat equation to wave and Klein-Gordon equation. However, the experiments involved only one-dimensional or two-dimensional wave-guide

*Institute of Computational Science, USI Lugano, CH-6904 Lugano, Switzerland.
E-mail: daniel.ruprecht@usi.ch. Supported by the Swiss HP2C initiative.

†Mathematisches Institut, Heinrich-Heine-Universität, D-40255 Düsseldorf, Germany.
E-mail: schaedle@am.uni-duesseldorf.de

‡ZIB Berlin, D-14195 Berlin, Germany.
E-mail: frank.schmidt@zib.de. Supported by the DFG Research Center MATHEON "Mathematics for key technologies" in Berlin.

geometries. The present paper extends this approach to the fully two-dimensional case and investigates its performance through numerical experiments. While the very good performance of the pole condition is confirmed in the two-dimensional case for Schrödinger's equation and the drift-diffusion equation, instabilities are found for the wave equation.

As the infinite element method, see [3], the pole condition does not truncate the exterior domain at some finite length. Nevertheless, the finite number of expansion coefficients of the Laplace transform also results in some form of truncation and the pole condition realizes a radiation boundary condition at the boundary of the interior domain and does not aim at providing a meaningful solution in the exterior. In some special cases, see [25], the pole condition is closely related to the perfectly matched layer approach introduced in [4], but as it does not require complex coordinate stretching, the pole condition provides a more general framework. Note that in contrast to other approaches to TBC involving Laplace transforms, for example [1], the pole condition applies the Laplace transform in space and not in time.

The class of problems considered are, as in [18], initial value problems for linear PDEs of the form

$$p(\partial_t)u(t, \mathbf{x}) = c^2 \Delta u(t, \mathbf{x}) - \mathbf{d} \cdot \nabla u(t, \mathbf{x}) - k^2 u(t, \mathbf{x}) \text{ for } \mathbf{x} \in \mathbb{R}^2, t \geq 0. \quad (1.1)$$

Included here are the Klein-Gordon equation for $p(\partial_t) = \partial_{tt}$ and $\mathbf{d} = (0, 0)^T$, the drift-diffusion equation for $p(\partial_t) = \partial_t$ and $k = 0$, the heat equation for $p(\partial_t) = \partial_t$ and $\mathbf{d} = (0, 0)^T$, $k = 0$ and finally Schrödinger's equation for $p(\partial_t) = i\partial_t$ and $\mathbf{d} = (0, 0)^T$, $k = 0$. Equation (1.1) is to be solved on a finite computational domain $\Omega \subset \mathbb{R}^2$ with some boundary condition $\mathbf{B}(u) = 0$ on $\partial\Omega$, such that on the domain Ω the solution of the initial boundary value problem approximates the solution of the unrestricted initial value problem.

If the support of the initial value $u(0, \mathbf{x})$ is a subset of Ω and the exterior domain is homogeneous, in the linear case the boundary condition has to suppress all modes traveling from the exterior $\mathbb{R}^2 \setminus \Omega$ into the computational domain. Section 2 illustrates the main concept of the pole condition by means of a simple one-dimensional example. Section 3 introduces the details of the discretization employed in the two-dimensional case and Section 4 shows several numerical examples.

2. Pole condition. This section provides a brief sketch of the key idea of the pole condition. Denote the Laplace transform of some function f along some (spatial) coordinate r by

$$\mathcal{L}(f)(s) = \int_0^\infty \exp(-sr) f(r) dr. \quad (2.1)$$

The pole condition exploits the identity

$$\exp(ar) \xrightarrow{\mathcal{L}} \frac{1}{s - a}, \quad (2.2)$$

that is a mode with phase a in physical space corresponds to a pole of the Laplace transform located at a . The poles of the Laplace transform of the solution are decomposed into poles corresponding to incoming and outgoing modes or, more generally, into poles corresponding to physical and non-physical modes. If the locations of the poles in the complex plane corresponding to these modes can be separated by a line, one can decompose the complex plane into a half-plane \mathbb{C}_{in} containing all incoming

TABLE 2.1
Region \mathbb{C}_{in} for different equations as derived in [18].

Equation	Parameters in (1.1)	\mathbb{C}_{in}
Schrödinger equation	$p(\partial_t) = i\partial_t, \mathbf{d} = 0, k = 0$	$\{z \in \mathbb{C} : \text{Re}(z) > -\text{Im}(z)\}$
Drift-diffusion equation	$p(\partial_t) = \partial_t, k = 0$	$\{z \in \mathbb{C} : \text{Re}(z) > 0\}$
Wave equation	$p(\partial_t) = \partial_{tt}, \mathbf{d} = 0, k = 0$	$\{z \in \mathbb{C} : \text{Im} < 0\}$
Klein-Gordon equation	$p(\partial_t) = \partial_{tt}, \mathbf{d} = 0$	$\{z \in \mathbb{C} : \text{Im} < 0\}$

modes and a half-plane \mathbb{C}_{out} containing all outgoing modes. Note that these half-planes depend on the equation at hand: Table 2.1 quotes the regions corresponding to the equations mentioned above as derived in [18]. For a given \mathbb{C}_{in} , the pole condition is then defined as follows:

DEFINITION 2.1. *Let $u(t, r)$ be a function depending on time t and some spatial coordinate r . Denote its Fourier transform in t by \hat{u} and the dual variable to t by ω . Then u satisfies the pole condition, if $U(\omega, s) := \mathcal{L}(\hat{u}(\omega, \cdot))(s)$ has an analytic extension to \mathbb{C}_{in} for every ω .*

To illustrate this concept, consider the one-dimensional wave equation on a semi-infinite interval

$$\partial_{tt}u(x, t) = \partial_{xx}u(x, t), \quad x \in \Omega = [-1, \infty) \quad (2.3)$$

and assume that a boundary condition at $x = 0$ is sought such that the solution of (2.3) coincides with the solution on the restricted domain $[-1, 0]$. Here, the r from Definition 2.1 is identical to the spatial coordinate x . Inserting an ansatz

$$u(x, t) = \exp(-i\omega t) \exp(ikx) \quad (2.4)$$

into (2.3) yields the dispersion relation

$$\omega = \pm k \quad (2.5)$$

and assuming $\omega > 0$ without loss of generality yields solutions of the form

$$u(x, t) = c_1 \exp(-i\omega t) \exp(i\omega x) + c_2 \exp(-i\omega t) \exp(-i\omega x), \quad (2.6)$$

where the first term corresponds to the positive branch of the dispersion relation and is rightward moving while the second term corresponds to the negative branch and is leftward moving. Let the non-physical modes in this example be the modes traveling leftwards from $(0, \infty)$ into the interval $[-1, 0]$. The pole condition then has to suppress the pole corresponding to the second term in (2.6).

In order to point out the connection between the two modes in (2.6) and their corresponding poles, we derive an equation for $U = \mathcal{L}(u)$ from (2.3). The Laplace transform satisfies the identity

$$\mathcal{L}(\partial_{xx}f)(s) = s^2\mathcal{L}(f)(s) - sf_0 - f'_0, \quad (2.7)$$

where f_0 and f'_0 denote the Dirichlet and Neumann data at $x = 0$. Further, as in Definition 2.1, denote by U the function obtained by applying to u Fourier transform in time and Laplace transform in space. Using (2.7), we obtain from (2.3) the equation

$$\begin{aligned} -\omega^2 U(\omega, s) &= s^2 U(\omega, s) - s\hat{u}_0(\omega) - \hat{u}'_0(\omega) \\ \Rightarrow U(\omega, s) &= \frac{1}{2} \frac{\hat{u}_0 - (i/\omega)\hat{u}'_0}{s - i\omega} + \frac{1}{2} \frac{\hat{u}_0 + (i/\omega)\hat{u}'_0}{s + i\omega}, \end{aligned} \quad (2.8)$$

where $\hat{u}_0(\omega)$, $\hat{u}'_0(\omega)$ are the Fourier transforms of the time-dependent Dirichlet and Neumann data $u_0(t)$, $u'_0(t)$ at $x = 0$. By (2.2), the first term with pole at $i\omega$ corresponds to the physically correct rightward propagating mode with coefficient c_1 in (2.6), the second term with pole at $-i\omega$ to the non-physical leftward traveling mode with coefficient c_2 . In order to exclude the non-physical mode, one could for example set $\mathbb{C}_{\text{in}} = \{z \in \mathbb{C} : \text{Im}(z) < 0\}$, so that the pole condition requires U to be analytic at $-i\omega$, thus removing this pole from U and the corresponding mode from the solution. Note that in this simple one-dimensional example, the pole condition can also be enforced by requiring the numerator of the right term in (2.8) to vanish, leading to

$$i\omega\hat{u}_0 + \hat{u}'_0 = 0 \leftrightarrow \partial_t u_0 - u'_0 = 0, \quad (2.9)$$

which is the well known transparent boundary condition for the one-dimensional wave equation, see for example [5].

For more complex problems, an explicit decomposition of U like (2.8) is usually not available. However, the Laplace transform can often still be decomposed into incoming and outgoing parts in terms of path integrals in the complex plane, see [18], hence still allowing to define a region \mathbb{C}_{in} and a pole condition based transparent boundary condition. In particular, this is possible for the different types of equations listed in Table 2.1.

3. Discretization. This section presents the employed discretizations. Subsection 3.1 describes the discretization of the exterior domain with special semi-infinite elements and how the pole condition is incorporated. The mapping between the exterior elements and the corresponding reference element introduces a generalized distance coordinate, along which the pole condition is enforced. As the exterior elements are semi-infinite, integrals arise that have one limit infinite. A mapping is introduced, converting these integrals into proper integrals in the Hardy space on the complex unit-disc. The discretization of the interior uses standard finite elements and is not elaborated further. Subsection 3.2 describes the employed integration schemes, including the choices of the parameter of the mappings.

3.1. Space discretization. The discretization of the exterior domain uses semi-infinite trapezoids as proposed in [24, 25]. The construction of these exterior meshes is discussed in [14]. Possible other choices would be semi-infinite triangles and rectangles as in [17]. In any case the exterior discretization has to be such that there is a uniform distance variable. For the sake of simplicity, we assume that the computational domain Ω is convex, although a generalization to star-shaped domains should be possible.

3.1.1. Transformation of exterior elements. We mainly use the notation of [17]. Figure 3.1 sketches the used mesh including the exterior elements and the mapping between the semi-infinite trapezoids in the exterior and the corresponding reference element. Each of the semi-infinite elements T is the image of the semi-infinite reference rectangle $[0, 1] \times [0, \infty)$ under the bilinear mapping \mathbf{g} for a set of parameters (h_η, h_ξ, a, b) . Denoting the Jacobian matrix of \mathbf{g} by J and its determinant by $|J|$, the mass and stiffness integrals of the variational formulation, which may be found in [17], are repeated below for the convenience of the reader. Additionally the

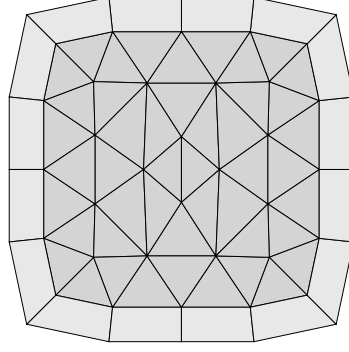


FIG. 3.1. Employed basic mesh. Elements triangulating the interior domain are marked in dark grey while the trapezoids decomposing the exterior are marked in light grey. Finer meshes are generated by uniform refinements of the triangles and adding additional rays and exterior elements when new nodes on the boundary emerge.

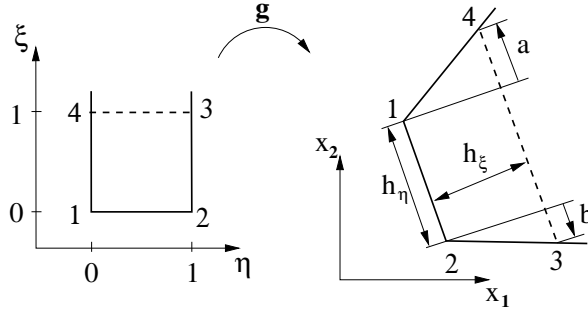


FIG. 3.2. Transformation mapping the reference semi-infinite rectangle to an exterior trapezoidal element.

drift term is given.

$$\begin{aligned}
 \int_T \nabla_{\mathbf{x}} u \cdot \nabla_{\mathbf{x}} v \, d\mathbf{x} &= \int_{[0,1] \times [0,\infty]} J^{-T} \nabla_{\eta\xi} \tilde{u} \cdot J^{-T} \nabla_{\eta\xi} \tilde{v} |J| \, d(\eta, \xi), \\
 \int_T \mathbf{d} \cdot \nabla_{\mathbf{x}} u \, v \, d\mathbf{x} &= \int_{[0,1] \times [0,\infty]} \mathbf{d} \cdot J^{-T} \nabla_{\eta\xi} \tilde{u} \, \tilde{v} |J| \, d(\eta, \xi), \\
 \int_T u \, v \, d\mathbf{x} &= \int_{[0,1] \times [0,\infty]} \tilde{u} \, \tilde{v} |J| \, d(\eta, \xi),
 \end{aligned} \tag{3.1}$$

The Jacobian of the bilinear mapping \mathbf{g} and its determinant are

$$J = R \begin{pmatrix} h_\eta + (a+b)\xi & -b + (a+b)\eta \\ 0 & h_\xi \end{pmatrix}, \quad |J| = h_\xi(h_\eta + (a+b)\xi), \tag{3.2}$$

where R is a rotation, h_η is the width of the trapezoid, h_ξ is a scaling factor measuring the distance to the boundary and a and b are signed distance variables, compare for Figure 3.2.

As in [17] we use a product ansatz $\tilde{u}(\eta, \xi) := u(\mathbf{g}(\eta, \xi)) = \tilde{u}_\xi(\xi) \tilde{u}_\eta(\eta)$ on the reference strip, where \tilde{u}_ξ and \tilde{u}_η are functions in ξ and η , respectively. The stiffness

term, for example, is given by

$$\begin{aligned} \int_{[0,1] \times [0,\infty]} J^{-T} \nabla_{\eta\xi} \tilde{u} \cdot J^{-T} \nabla_{\eta\xi} \tilde{v} |J| d(\eta, \xi) = \\ \int_0^1 \int_0^\infty \begin{pmatrix} \partial_\eta \tilde{u}_\eta \tilde{u}_\xi \\ \tilde{u}_\eta \partial_\xi \tilde{u}_\xi \end{pmatrix}^T \begin{pmatrix} \frac{h_\xi^2 + (b - (a+b)\eta)^2}{h_\eta + \xi(a+b)} & \frac{b - (a+b)\eta}{h_\xi} \\ \frac{b - (a+b)\eta}{h_\xi} & \frac{h_\eta + (a+b)\xi}{h_\xi} \end{pmatrix} \begin{pmatrix} \partial_\eta \tilde{v}_\eta \tilde{v}_\xi \\ \tilde{v}_\eta \partial_\xi \tilde{v}_\xi \end{pmatrix} d\xi d\eta. \end{aligned} \quad (3.3)$$

Functions \tilde{u}_η will be approximated using standard finite element basis functions $\{\phi_j(\eta)\}$, $j = 1, \dots, N_\eta$ and therefor integrals over the radial coordinate η can be evaluated by quadrature formulas.

3.1.2. Hardy Space. Infinite integrals over the radial coordinate ξ are transformed to finite integrals in the Hardy space $H^+(D_0)$ using the identity

$$\int_0^\infty \tilde{f}(\xi) \tilde{g}(\xi) d\xi = -2s_0 \frac{1}{2\pi} \int_{\partial D_0} (\mathcal{M}\mathcal{L}f)(\bar{z})(\mathcal{M}\mathcal{L}g(z)) |dz| \quad (3.4)$$

where \mathcal{M} denotes the modified Möbius transform

$$H^-(P_{s_0}) \rightarrow H^+(D_0) : F \mapsto \mathcal{M}F \text{ defined by } (\mathcal{M}F)(z) := F\left(s_0 \frac{z+1}{z-1}\right) \frac{1}{z-1}. \quad (3.5)$$

Here, P_{s_0} denotes a half-plane in the complex plane, depending on the parameter s_0 , and D_0 denotes the complex unit-disc, see Figure 3.3. Further, \mathcal{M} is an isomorphism between the Hardy spaces $H^-(P_{s_0})$ and $H^+(D_0)$. Details can be found in [16, 17].

The parameter s_0 has to be chosen such that the half-plane P_{s_0} coincides with the half-plane \mathbb{C}_{in} of non-physical poles for the considered problem. As functions in the space $H^-(P_{s_0})$ are analytic on the half-plane P_{s_0} and \mathcal{M} is an isomorphism, a function $\mathcal{M}F$ is analytic on D_0 if and only if F is analytic on P_{s_0} .

Hence the pole condition, stating that the Laplace transform $\mathcal{L}(f)$ of some function f has to be analytic on \mathbb{C}_{in} , is equivalent to the condition that $\mathcal{M}\mathcal{L}(f)$ is analytic on D_0 for the correct choice of the parameter s_0 . In short, we established the following sequence of reformulations of the pole condition

$$\begin{aligned} f \text{ satisfies pole condition} &: \Leftrightarrow F \text{ has analytic extension to } \mathbb{C}_{\text{in}} \\ &\Leftrightarrow F \in H^-(P_{s_0}) \text{ for correct choice of } s_0 \\ &\Leftrightarrow \mathcal{M}F \in H^+(D_0), \end{aligned} \quad (3.6)$$

see [16] for details.

In order to derive a formulation, which is easy to implement, some more transformations are required: Given a function f , its image under \mathcal{L} and \mathcal{M} is decomposed into

$$\mathcal{M}\mathcal{L}(f)(z) = \frac{1}{2s_0}(f_0 + (z-1)F(z)) =: \frac{1}{s_0} \mathcal{T}_- \begin{pmatrix} f_0 \\ F \end{pmatrix} (z) \quad (3.7)$$

in order to get a local coupling with the boundary data f_0 . As the Laplace transform maps differentiation to multiplication by $s_0(z+1)/(z-1)$, straightforward calculation yields

$$\mathcal{M}\mathcal{L}(f')(z) = \frac{1}{2}(f_0 + (z+1)F(z)) =: \mathcal{T}_+ \begin{pmatrix} f_0 \\ F \end{pmatrix} (z). \quad (3.8)$$

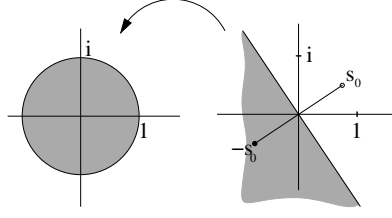


FIG. 3.3. Sketch of the Möbius transform $\mathcal{M} : H^-(P_{s_0}) \rightarrow H^+(D_0)$, mapping functions defined on the complex half-plane P_{s_0} to functions defined on the complex unit-disc D_0 . The parameter s_0 has to be chosen such that P_{s_0} corresponds to the \mathbb{C}_{in} suitable for the problem at hand.

For motivating this coupling, note that it follows from general theory on Laplace transforms that if F is the Laplace transform of f one has $\lim_{s \rightarrow \infty} sF(s) = f(0)$, whenever $f(0)$ exists. For details on the decomposition we again refer to [16, 17].

It remains to take care of terms which contain multiplications by ξ and $((a + b)\xi + h_\eta)^{-1}$ in (3.3). To this end, an additional operator $\mathcal{P} : H^+(D_0) \rightarrow H^+(D_0)$ (multiplication by ξ)¹ is implicitly defined by

$$\mathcal{M}\mathcal{L}\{(\cdot)f(\cdot)\} = \mathcal{M}\{-(\mathcal{L}f(\cdot))'\} = s_0^{-1}\mathcal{P}(\mathcal{M}\mathcal{L}f).$$

Direct calculations yield

$$(\mathcal{P}F)(z) = \frac{(z-1)^2}{2}F'(z) + \frac{z-1}{2}F(z), \quad F \in H^+(D_0). \quad (3.9)$$

Assembling the discrete system involves basically the assembly of discrete counterparts of the operators \mathcal{T}_+ , \mathcal{T}_- and \mathcal{P} .

3.1.3. Choosing Basis Functions. Up to now, all transformations were on a continuous level and no approximations were made. Because functions that are analytic on the complex unit-disc can be expanded in power series, the set of monomials $\{z^j\}_{j=0}^\infty$ constitutes a basis of $H^+(D_0)$. By using the space spanned by a finite number of monomials $\{z^j\}_{j=0}^{N_\xi}$ as test and ansatz space, one obtains finite dimensional approximations of \mathcal{T}_\pm

$$T_{N_\xi,+} = \begin{pmatrix} 1 & 1 & & \\ & 1 & 1 & \\ & & \ddots & \ddots \\ & & & 1 \end{pmatrix}, \quad T_{N_\xi,-} = \begin{pmatrix} 1 & -1 & & \\ & 1 & -1 & \\ & & \ddots & \ddots \\ & & & 1 \end{pmatrix}, \quad (3.10)$$

and \mathcal{P}

$$P_{N_\xi} = \begin{pmatrix} -1 & 1 & & \\ 1 & -3 & 2 & \\ & \ddots & \ddots & \ddots \\ & & (N_\xi - 1) & -(2N_\xi + 1) \end{pmatrix}. \quad (3.11)$$

The Hardy space monomials can also be transformed back to give a representation of the corresponding ansatz and test functions in physical space, see [16]. To define the

¹This operator is denoted by D in [17].

local stiffness matrix, set for the ξ -integrals

$$\begin{aligned} L_{\xi,11}^{(-1)} &:= -2 T_{N_{\xi},-}^{\top} \left(h_{\eta} s_0 I + (a+b) P_{N_{\xi}} \right)^{-1} T_{N_{\xi},-}, \\ L_{\xi,12}^{(0)} &:= -2 T_{N_{\xi},-}^{\top} T_{N_{\xi},+}, \quad L_{\xi,21}^{(0)} := -2 T_{N_{\xi},+}^{\top} T_{N_{\xi},-}, \\ L_{\xi,22}^{(1)} &:= -2 h_{\eta} T_{N_{\xi},+}^{\top} T_{N_{\xi},+}, \quad L_{\xi,22}^{(0)} := -2(a+b) T_{N_{\xi},+}^{\top} P_{N_{\xi}} T_{N_{\xi},+}. \end{aligned} \quad (3.12)$$

Here the superscript counts the leading order in s_0 and the subscripts correspond to the position in the matrix in (3.3). For the η -integrals set

$$\begin{aligned} L_{\eta,11} &:= \left(\int_0^1 \phi'_i(\eta) \left(h_{\xi} + \frac{((a+b)\eta - b)^2}{h_{\xi}} \right) \phi'_j(\eta) \right)_{i,j=1}^{N_{\eta}}, \\ L_{\eta,12} &:= \left(\int_0^1 \phi'_i(\eta) \frac{b - (a+b)\eta}{h_{\xi}} \phi_j(\eta) \right)_{i,j=1}^{N_{\eta}}, \\ L_{\eta,21} &:= \left(\int_0^1 \phi_i(\eta) \frac{b - (a+b)\eta}{h_{\xi}} \phi'_j(\eta) \right)_{i,j=1}^{N_{\eta}}, \\ L_{\eta,22} &:= \left(\int_0^1 \phi_i(\eta) \frac{1}{h_{\xi}} \phi_j(\eta) \right)_{i,j=1}^{N_{\eta}}. \end{aligned} \quad (3.13)$$

For equations with second order temporal derivatives, the parameter s_0 is chosen to be frequency dependent in Fourier space, to be precise $s_0 = i\omega$, translating back to ∂_t in physical space. To avoid the inversion in $L_{\xi,11}^{(-1)}$ in (3.12), additional unknowns are introduced such that the local stiffness matrices are given by

$$\begin{aligned} L_{loc}^{(0)} &= \begin{bmatrix} L_{\eta,22} \otimes L_{\xi,22}^{(0)} + L_{\eta,12} \otimes L_{\xi,12}^{(0)} + L_{\eta,21} \otimes L_{\xi,21}^{(0)} & -2L_{\eta,11} \otimes T_{N_{\xi},-}^{\top} \\ 2I \otimes T_{N_{\xi},-} & -2I \otimes (a+b)M_{N_{\xi}} \end{bmatrix} \\ L_{loc}^{(1)} &= \begin{bmatrix} L_{\eta,22} \otimes L_{\xi,22}^{(1)} & 0 \\ 0 & -2I \otimes h_{\eta} I \end{bmatrix}. \end{aligned} \quad (3.14)$$

Similarly, local mass matrices corresponding to the mass integral in (3.1) are given by

$$M_{loc}^{(-1)} := \begin{bmatrix} M_{\xi}^{(-1)} \otimes M_{\eta} & 0 \\ 0 & 0 \end{bmatrix}, \quad M_{loc}^{(-2)} := \begin{bmatrix} M_{\xi}^{(-2)} \otimes M_{\eta} & 0 \\ 0 & 0 \end{bmatrix} \quad (3.15)$$

where

$$\begin{aligned} M_{\xi}^{(-1)} &:= -2h_{\xi} h_{\eta} T_{N_{\xi},-}^{\top} T_{N_{\xi},-} \quad \text{and} \quad M_{\eta} := \left(\int_0^1 \phi_i(\eta) \phi_j(\eta) \right)_{i,j=1}^{N_{\eta}}, \\ M_{\xi}^{(-2)} &:= -2h_{\xi} (a+b) T_{N_{\xi},-}^{\top} P_{N_{\xi}} T_{N_{\xi},-} \end{aligned} \quad (3.16)$$

For the drift term set

$$\begin{aligned} D_{\xi,1}^{(0)} &:= -2T_{N_{\xi},-}^{\top} T_{N_{\xi},+} \\ D_{\xi,2}^{(-1)} &:= -2(a+b) T_{N_{\xi},-}^{\top} P_{N_{\xi}} T_{N_{\xi},+} \\ D_{\xi,3}^{(-1)} &:= -2T_{N_{\xi},-}^{\top} T_{N_{\xi},-} \end{aligned} \quad (3.17)$$

and

$$\begin{aligned}
D_{\eta,1} &:= h_\eta \tilde{d}_2 \left(\int_0^1 \phi_i(\eta) \phi_j(\eta) \right)_{i,j=1}^{N_\eta} \\
D_{\eta,2} &:= \tilde{d}_2 \left(\int_0^1 \phi_i(\eta) \phi_j(\eta) \right)_{i,j=1}^{N_\eta} \\
D_{\eta,3} &:= \left(\int_0^1 \phi_i(\eta) (\tilde{d}_2(b - (a+b)\eta) + \tilde{d}_1 h_\xi) \phi'_j(\eta) \right)_{i,j=1}^{N_\eta}
\end{aligned} \tag{3.18}$$

where $(\tilde{d}_1, \tilde{d}_2)^T = \tilde{\mathbf{d}} = R\mathbf{d}$ is the rotated \mathbf{d} vector. The local drift matrices are then given by

$$D_{loc}^{(0)} := \begin{bmatrix} D_{\xi,1}^{(0)} \otimes D_{\eta,1} & 0 \\ 0 & 0 \end{bmatrix}, D_{loc}^{(-1)} := \begin{bmatrix} D_{\xi,2}^{(-1)} \otimes D_{\eta,2} + D_{\xi,3}^{(-1)} \otimes D_{\eta,3} & 0 \\ 0 & 0 \end{bmatrix} \tag{3.19}$$

In the computational domain Ω standard local finite element matrices $M_{loc}^{(0)}, D_{loc}^{(0)}, L_{loc}^{(0)}$ without the s_0 -parameter are obtained. By assembling the local matrices to global matrices, a spatial semi-discretization of (1.1) is obtained

$$\begin{aligned}
p(\partial_t) \left(M^{(0)} + \frac{1}{s_0} M^{(-1)} + \frac{1}{s_0^2} M^{(-2)} \right) u(t) &= \left(L^{(0)} + s_0 L^{(1)} \right) u(t) + \\
\left(D^{(0)} + \frac{1}{s_0} D^{(-1)} \right) u(t) - k^2 \left(M^{(0)} + \frac{1}{s_0} M^{(-1)} + \frac{1}{s_0^2} M^{(-2)} \right) u(t)
\end{aligned} \tag{3.20}$$

where $u(t)$ is the time-dependent vector of degrees-of-freedom, including the coefficients of the monomial basis functions of the subset of $H^+(D_0)$ providing the boundary condition.

3.2. Time discretization. All conducted simulations rely on the method-of-lines approach: The PDE at hand is first discretized in space, as described in subsection 3.1, leading to the ODE (3.20) for the coefficients. This equation is then integrated in time using different time-stepping schemes indicated below.

3.2.1. Schrödinger's equation. For Schrödinger's equation, (3.20) is solved by the second order accurate, A-stable trapezoidal/mid-point rule. Denoting by u^n the approximation to $u(nh)$ at $t = nh$ for some time-step size h , the discretization reads

$$\partial_t M u(t) = -ic^2 L u(t) \leftrightarrow M \frac{u^{n+1} - u^n}{h} = -ic^2 L \frac{u^{n+1} + u^n}{2} \tag{3.21}$$

where the mass and stiffness matrix are given by $M = M^{(0)} + s_0^{-1} M^{(-1)} + s_0^{-2} M^{(-2)}$ and $L = L^{(0)} + s_0 L^{(1)}$. As in the one-dimensional case, non-physical solutions correspond to poles in the first quadrant, hence s_0 is chosen in the third quadrant and set to

$$s_0 = -1 - i, \tag{3.22}$$

in order to exclude poles in the region \mathbb{C}_{in} indicated in Table 2.1.

3.2.2. Drift-Diffusion equation. In the examples for the drift-diffusion equation, (3.20) is integrated with the A-stable Radau IIA method with three stages of order five, see [10, Sec. IV.5]. The parameter s_0 is chosen to be real and negative, such that the poles in the positive half-plane are excluded, corresponding to non-physical exponentially increasing solutions. We set

$$s_0 = -5, \quad (3.23)$$

hence poles with positive real part, see Table 2.1, are excluded. The chosen value of s_0 produces good results, but some optimization is probably still possible. However, the sensitivity of the results to the specific value is rather low, as long as the correct half-plane is excluded.

3.2.3. Wave equation. For the wave equation, poles in the lower complex half-plane have to be excluded, see 2.1. For the wave equation it is $p(\partial t) = \partial_{tt}$, corresponding to $p(\omega) = -\omega^2$ in frequency space. As in the one-dimensional case, we choose the parameter s_0 to be frequency dependent, setting

$$s_0 = i\omega. \quad (3.24)$$

Transforming back to physical space yields

$$\partial_{tt}M^{(0)}u - \partial_tM^{(-1)}u + M^{(-2)}u = L^{(0)}u - \partial_tL^{(1)}u. \quad (3.25)$$

Discretization is done again with the implicit trapezoidal rule, resulting in

$$\begin{aligned} M^{(0)} \frac{u^{n+1} - 2u^n + u^{n-1}}{h^2} - M^{(-1)} \frac{u^{n+1} - u^{n-1}}{2h} + M^{(-2)} \frac{u^{n+1} + 2u^n + u^{n-1}}{4} = \\ L^{(0)} \frac{u^{n+1} + 2u^n + u^{n-1}}{4} - L^{(1)} \frac{u^{n+1} - u^{n-1}}{2h}. \end{aligned} \quad (3.26)$$

4. Numerical results. The computational domain in all simulations is a square $[-4, 4] \times [-4, 4]$ in the two-dimensional plane with slightly smoothed corners, see Figure 3.1. Sketched in light gray are the trapezoidal elements spanned by the rays in the exterior domain while the darker triangles correspond to the triangulation of the interior domain. In order to obtain higher resolutions, the shown mesh is refined using up to five uniform refinement steps. As the original mesh is very coarse, no errors are reported for simulations on the unrefined grid, because at least lower order finite elements do not produce reasonable solutions there.

4.1. Schrödinger's equation. For $p(\partial_t) = i\partial_t$, $c = k = 0$ and $\mathbf{d} = (0, 0)^T$, equation (1.1) yields Schrödinger's equation. For this case, exact solutions of the form

$$u_\alpha(x, y, t; \alpha) = \frac{i}{4t + i} \exp\left(\frac{-i(x^2 + y^2) - \alpha(x + y) - 2\alpha^2 t}{4t + i}\right) \quad (4.1)$$

with a parameter α are available. We use a superposition of two such solutions, that is

$$u(x, y, t) = u_\alpha(x, y, t; \alpha = 1.4) + u_\alpha(x, y, t; \alpha = -2), \quad (4.2)$$

and employ $u(x, y, 0)$ as initial value. The discretization in space employs finite elements of orders one to four in the interior. Simulations are run until $T = 10$ with

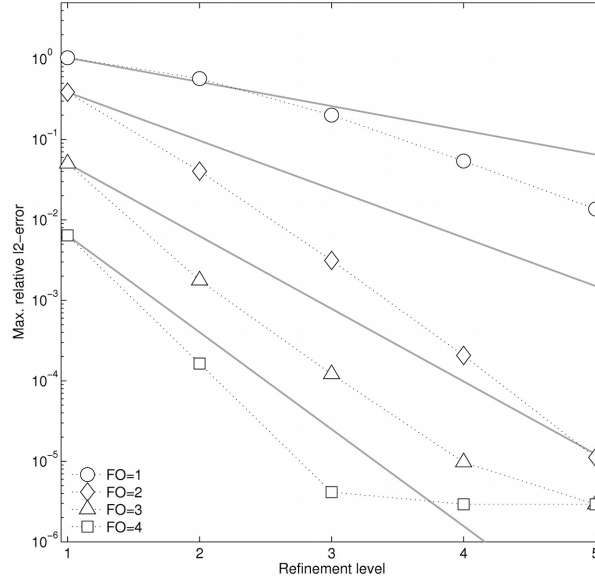


FIG. 4.1. Verification of the spatial order of convergence for the Schrödinger equation. Shown is the maximum of the relative l_2 -errors over all outputs versus the refinement level of the mesh for finite elements of order one to four. The employed time-step is $\Delta t = 1/6000$ and $N_\xi = 20$ coefficients along each ray are used. As a guide to the eye, lines with slopes one to four have been added.

time-step	$\log_{10}(\text{error})$	Conv. Rate
1/800	-3.8	—
1/1600	-4.4	2.0
1/3200	-5.0	2.0
1/6000	-5.5	2.0

TABLE 4.1

Maximum relative l_2 -error over all generated outputs for the Schrödinger equation, depending on the time-step size. The simulation used finite elements of order four, a five times refined mesh and $N_\xi = 20$ coefficients along each exterior ray.

time-steps $\Delta t = 1/800, 1/1600, 1/3200, 1/6000$ on meshes refined up to five times and for values of N_ξ (coefficients per ray) between $N_\xi = 1$ and $N_\xi = 20$. Output is generated at two hundred points in time, distributed equally over the time interval $[0, 10]$.

Figure 4.1 shows the maximum relative l_2 -error over all generated outputs versus the refinement levels of the mesh for finite elements of order one to four. All elements converge with the expected rate or better until the error saturates at about 3×10^{-6} in the case of the higher order finite elements. At this point, the error from the temporal discretization starts dominating, compare for Table 4.1, and increasing the accuracy of the spatial discretization yields no more improvement unless the accuracy of the time-discretization is also increased.

Table 4.1 shows the maximum relative l_2 -error versus the length of the time-step, confirming the convergence rate of two expected from the employed second order accurate trapezoidal rule.

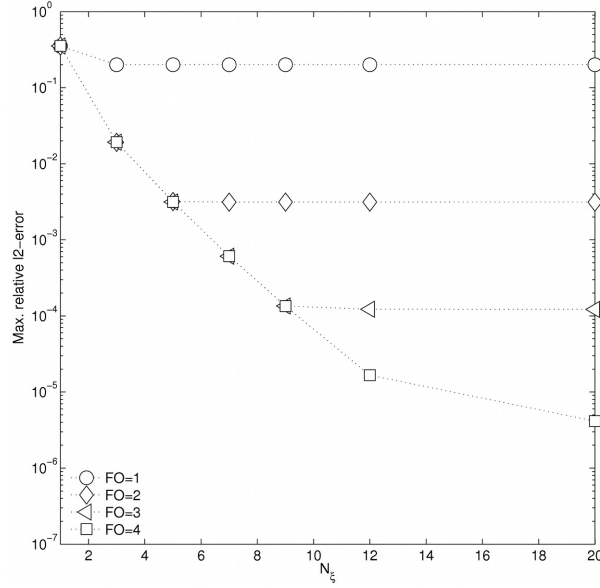


FIG. 4.2. Relative l_2 -error depending on the number of coefficients N_ξ per ray in the exterior domain for Schrödinger's equation. Maximum error over all generated outputs for finite elements of order one to four on a three times refined mesh.

Figures 4.2 and 4.3 show how the error decays with increasing N_ξ . The former shows the maximum relative l_2 -error for simulations with finite elements of order one to four, a three times refined mesh and a time-step of $\Delta = 1/6000$. In all cases, the error decays super-algebraically with N_ξ until it saturates at the level of the respective spatial or temporal discretization error. Figure 4.3 shows the error at four different points in time for the fourth order elements. The error decays super-algebraically at all four points in time, even at later times where most of the solution has left the domain.

Figure 4.4 shows the relative l_2 -error over time for different values of N_ξ . In all cases, the error increases as the wave packets hit the boundary of the computational domain and subsequently decays to a level determined by the number of coefficients per ray N_ξ . The error decays faster for larger values of N_ξ , but for values of $N_\xi = 10$ or larger, the levels at which the error saturates and in particular the error at the end of the simulation is identical.

4.2. Drift-diffusion equation. Setting $p(\partial_t) = \partial_t$ and $k = 0$ in (1.1) yields the drift-diffusion equation. Note that the heat equation is included here as the special case $\mathbf{d} = (0, 0)^T$. An analytic solution is given by

$$u(x, y, t) = \frac{1}{t} \exp \left(-\frac{1}{4tc^2} \left[(x - d_1 t)^2 + (y - d_2 t)^2 \right] \right). \quad (4.3)$$

Set

$$\mathbf{d} = (d_1, d_2) = (1.5, 1.5), \quad \text{and } c = 0.5 \quad (4.4)$$

and start the integration at $t_0 = 0.2$ with initial value $u(x, y, t_0)$. This yields a Gaussian function with a peak initially close to the origin which is subsequently

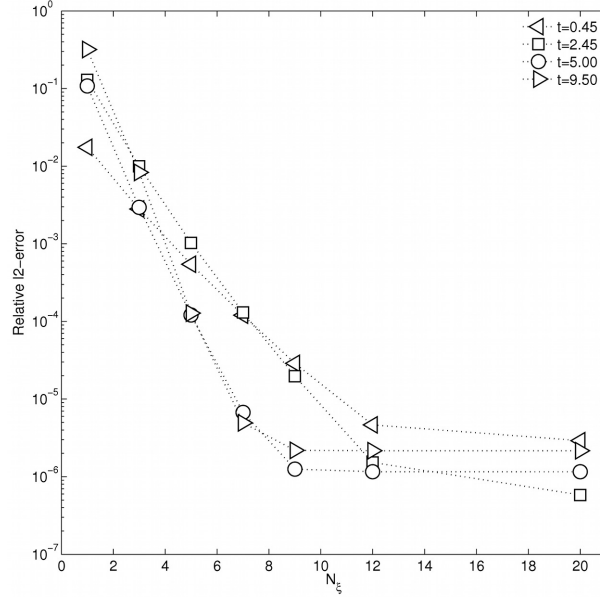


FIG. 4.3. Relative l_2 -error at four fixed points in time depending on the number of coefficients N_ξ per ray for the simulation with finite elements of order four. In all cases, a time-step of $\Delta = 1/6000$ has been used.

time-step	$\log_{10}(\text{error})$	Conv. Rate
1/10	-3.6	—
1/20	-5.0	4.6
1/30	-5.9	4.9
1/40	-6.5	4.9
1/60	-7.4	4.9
1/80	-8.0	5.0
1/160	-9.2	4.0

TABLE 4.2

Maximum relative l_2 -error over all generated outputs depending on the time-step size for finite elements of order six, a four times refined mesh and $N_\xi = 51$ coefficients per ray.

advected to the upper right corner of the square while being spread out by diffusion. Integration in time is done by the fifth order Radau IIA(5) scheme. The simulations are run until $T = 5$ with finite elements of order one to six, on meshes refined up to four times, values of N_ξ between 1 and 51 and time-steps ranging from $\Delta = 1/10$ to $\Delta t = 1/160$.

Figure 4.5 shows the maximum relative l_2 -error over all generated outputs versus the refinement level of the mesh. The number of coefficients per ray is $N_\xi = 51$ and the time-step is $\Delta t = 1/160$. As a guide to the eye, lines with slopes from one to six are added. All elements converge with the expected rate or better, confirming again that the pole condition does not compromise the order of convergence of the spatial discretization.

Table 4.2 shows the maximum relative l_2 -error versus the length of the employed time-step for finite elements of order six, a four times refined mesh and $N_\xi = 51$.

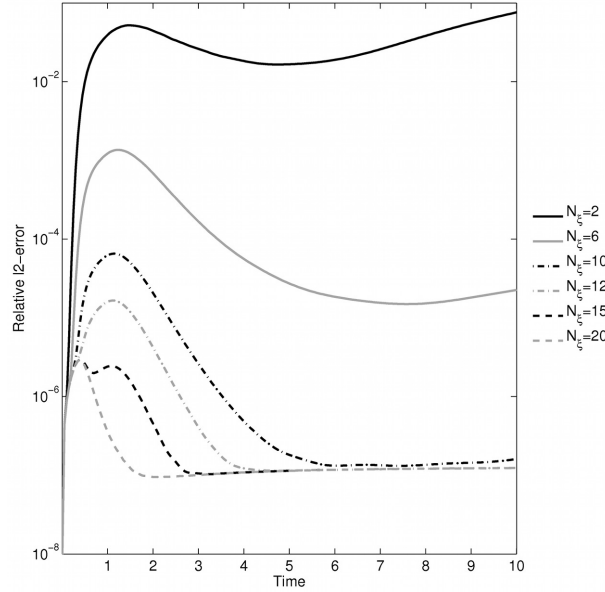


FIG. 4.4. Relative l_2 -error over time for the Schrödinger equation for six different values of N_ξ . The simulation used finite elements of order four, a five times refined mesh and a time-step $\Delta t = 1/6000$.

From $\Delta t = 1/10$ to $\Delta t = 1/20$, a slightly reduced convergence rate is observed, probably because the time-step size is still in the pre-asymptotic regime. The reduced convergence rate in the last refinement is because the error approaches the spatial discretization error, see Figure 4.5. Beside that, the expected fifth order convergence is observed, demonstrating that the pole condition can not only preserve the accuracy of high order finite elements but also of high order integration schemes.

Figures 4.6 and 4.7 show the relative l_2 -error versus the number of coefficients N_ξ . The former shows the maximum error over all outputs for finite elements of order one to six, a three times refined mesh and a time-step $\Delta t = 1/160$. In contrast to Schrödinger's equation, for small values of N_ξ there is only a minor decrease of the error. Also, below N_ξ , the error is not decreasing monotonically with the number of coefficients. After $N_\xi = 10$, rapid super-algebraically decrease of the error is again observed until the error saturates at a level determined by the accuracy of the spatial discretization. Note that $N_\xi = 30$ coefficients per ray are sufficient here to reduce the boundary condition error to the level of the spatial discretization error in all cases. Figure 4.7 shows the relative error at four different points in time. Again the error generally decays super-algebraically with the number of coefficients, but now the decay rates are noticeably lower at later points in time. Note that at $t = 0.43$, the Gauss peak has not yet reached the boundary, so that the boundary condition has no visible effect on the error at this time.

Figure 4.8 shows the relative l_2 -error over time for different values of N_ξ , finite elements of order six and a four times refined mesh. As for Schrödinger's equation, the error starts increasing at some point in time, but the increase starts later as the number of coefficients increases. On the other hand, for the simulations with $N_\xi = 15$ or less coefficients, the errors at the end of the simulation are about the same and

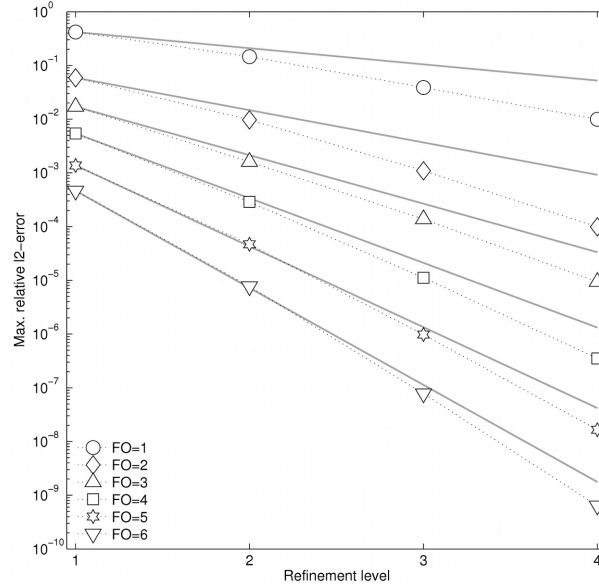


FIG. 4.5. Verification of the spatial order of convergence for the drift-diffusion equation integrated until $T = 5$. Shown is the maximum of the relative l_2 -errors over all generated outputs. The number of coefficients per ray is $N_\xi = 51$ and the time-step is $\Delta t = 1/160$.

only for larger values of N_ξ a significantly reduced error is observed at the end of the simulation. Together with Figure 4.6, this illustrates that for the drift-diffusion example, the error is not monotonically decreasing with N_ξ for small values of N_ξ and a certain minimum number of coefficients per ray is required before the onset of the super-algebraic decay.

4.3. Wave and Klein-Gordon equation. For $p(\partial_t) = \partial_{tt}$ and $\mathbf{d} = (0, 0)^T$, (1.1) becomes the Klein-Gordon equation, containing the wave equation as the special case $k = 0$. While the pole condition could successfully provide TBCs for both equations in the one-dimensional case as well as in a two-dimensional wave-guide problem, stability problems arise in the fully two-dimensional case, rendering the pole condition in the here presented form inapplicable to both equations for finite elements of order two or higher. Resolving these issues is planned for future research.

Below, the instability is documented briefly. Use an initial distribution

$$u(x, y) = \exp(-2x^2 - 2y^2), \quad (4.5)$$

finite elements of order one to four and up to four refinement steps for the mesh. Integrate in time using implicit trapezoidal rule with a time-step $\Delta t = 1/1280$ until $T = 100$.

Figure 4.9 shows the maximum l_2 -error over all generated outputs versus the size of the elements of the employed mesh for finite elements of order one to four. In order to obtain a readable plot, the error is capped at 10^1 and values of 10 correspond to unstable runs. While first order elements are stable on all five meshes, showing again better than expected convergence, for higher order elements and fine meshes, the method becomes unstable. Second order elements are unstable only on the finest mesh while third and fourth order elements already become unstable after three or

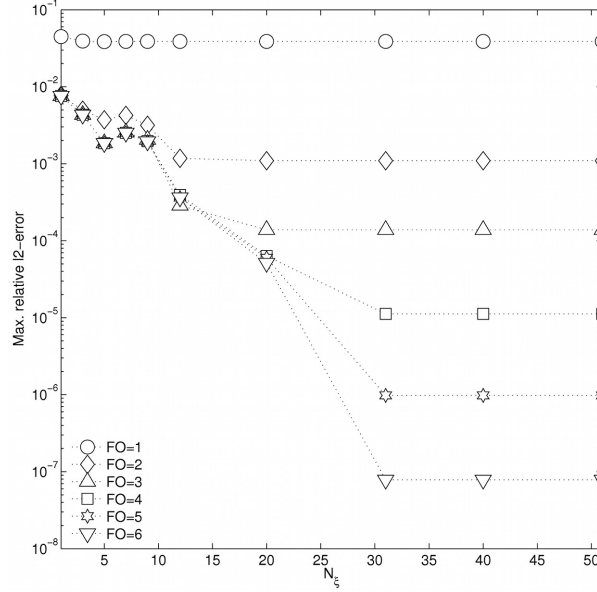


FIG. 4.6. Relative l_2 -error depending on the number of coefficients N_ξ per ray in the exterior domain for the drift-diffusion equation. Maximum error over all generated outputs for finite elements of order one to six on a three times refined mesh.

two refinement steps. Note that on the coarser meshes where the method is stable, the expected or better decay rates of the error are observed. Similar behavior is found for the Klein-Gordon equation, but not documented here.

Figure 4.10 shows the energy of the discrete solution over time for different values of N_ξ on the finest mesh for finite elements of order two. The simulations are stable for $N_\xi = 4$. They are also stable until about $t = 20$ for $N_\xi = 6, 10, 12, 15$, but an exponential instability occurs after this point in time. The instability also occurs when the simulation is run on a circular domain. Note that the employed integration scheme is A-stable, so that the instability on a finer mesh is not arising from a violation of some CFL-type stability limit.

5. Conclusions. The pole condition approach to transparent boundary conditions, derived in [18] for the time-dependent, one-dimensional case, is extended to time-dependent two-dimensional problems. The pole condition identifies in- and outgoing modes by associating them with poles of the spatial Laplace transform in the complex plane. The complex plane is then divided into two half-planes, \mathbb{C}_{in} and \mathbb{C}_{out} , containing the poles corresponding to incoming and outgoing modes respectively. To suppress modes traveling from the exterior into the computational domain, the Laplace transform is required to be analytic in \mathbb{C}_{in} . In order to obtain a numerically implementable formulation, \mathbb{C}_{in} is mapped to the unit circle by a conformal Möbius transformation. The Laplace transform is then extended in a power series on the unit circle with the coefficients of the expansion being connected to the interior degrees of freedom on the boundary. Truncating the series after a finite number of terms yields an approximate and implementable TBC.

Numerical examples are presented in order to investigate the performance of the pole condition approach: As in the 1D-case, the considered generic PDE contains

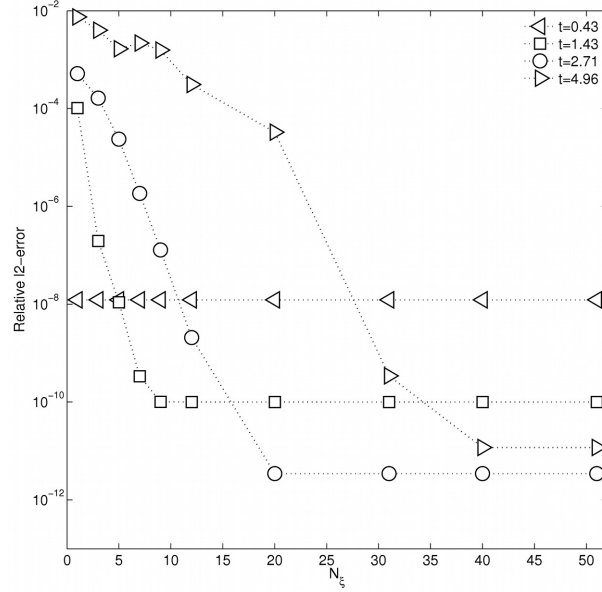


FIG. 4.7. Relative l_2 -error depending on N_s at four fixed points in time for the simulation with finite elements of order six. In all cases, a time-step $\Delta t = 1/160$ has been used.

different well-known equations for specific choices of parameters. Excellent results are obtained for Schrödinger's equation and the drift-diffusion equation: The presented numerical experiments demonstrate that the convergence order of finite elements up to order six is retained and also that the convergence order of the temporal discretization is not affected if sufficiently many coefficients are used for the boundary condition. Further it is shown that the error introduced by the approximate boundary condition decays super-algebraically as the number of coefficients in the expansion of the Laplace transform increases. For the drift-diffusion equation, a small minimal number of coefficients was found to be required to reach the regime of super-algebraic error decay.

Unfortunately, in contrast to the one-dimensional case, the approach exhibits instabilities for the two-dimensional wave and Klein-Gordon equation if using finite elements of order two or higher. Hence in the present form the pole condition is of limited use for these second order hyperbolic equations. A further investigation of the instability and hopefully a remedy will be subject of future research.

REFERENCES

- [1] B. ALPERT, L. GREENGARD, AND T. HAGSTROM, *Rapid evaluation of nonreflecting boundary kernels for time-domain wave propagation*, SIAM J. Numer. Anal., 37 (2000), pp. 1138–1164.
- [2] X. ANTOINE, A. ARNOLD, C. BESSE, M. EHRHARDT, AND A. SCHÄDLE, *A review of transparent and artificial boundary conditions techniques for linear and nonlinear Schrödinger equations*, Commun. Comput. Phys., 4 (2008), pp. 729–796.
- [3] R. ASTLEY, *Infinite elements for wave problems: A review of current formulations and an assessment of accuracy*, Int. J. Numer. Methods Eng., 49 (2000), pp. 951–976.
- [4] J.-P. BÉRENGER, *A perfectly matched layer for the absorption of electromagnetic waves*, J. Comput. Phys., 114 (1994), pp. 185–200.

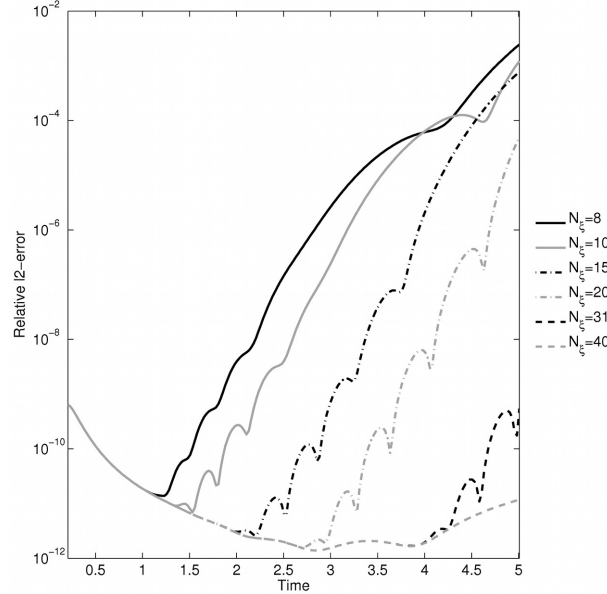


FIG. 4.8. Relative l_2 -error over time for the drift-diffusion equation for different values of N_x at a four times refined mesh, finite elements of order six and a time-step $\Delta t = 1/160$.

- [5] B. ENGQUIST AND A. MAJDA, *Absorbing boundary conditions for the numerical simulation of waves*, Math. Comp., 31 (1977), pp. 629–651.
- [6] M. GANDER AND A. SCHÄDLE, *The pole condition: A Padé approximation of the Dirichlet to Neumann operator*, in Domain decomposition methods in Science and Engineering XV, Lecture Notes in Computational Science and Engineering, Springer Verlag, 2010.
- [7] D. GIVOLI, *Non-reflecting boundary conditions*, J. Comput. Phys., 94 (1991), pp. 1–29.
- [8] ———, *High-order local non-reflecting boundary conditions: a review*, Wave Motion, 39 (2004), pp. 319–326.
- [9] T. HAGSTROM, *Radiation boundary conditions for numerical simulation of waves*, Acta Numerica, 8 (1999), pp. 47–106.
- [10] E. HAIRER AND G. WANNER, *Solving Ordinary Differential Equations II*, Springer Verlag, Berlin, Heidelberg, 1991.
- [11] T. HOHAGE AND L. NANNEN, *Hardy space infinite elements for scattering and resonance problems*, SIAM J. Numer. Anal., 47 (2009), pp. 972–996.
- [12] T. HOHAGE, F. SCHMIDT, AND L. ZSCHIEDRICH, *Solving Time-Harmonic Scattering Problems Based on the Pole Condition I: Theory*, SIAM J. Math. Anal., 35 (2003), pp. 183–210.
- [13] ———, *Solving Time-Harmonic Scattering Problems Based on the Pole Condition II: Convergence of the PML Method*, SIAM J. Math. Anal., 35 (2003), pp. 547–560.
- [14] B. KETTNER AND F. SCHMIDT, *Meshing of heterogeneous unbounded domains*, in Proceedings of the 17th Int. Meshing Roundtable, R. V. Garimella, ed., Springer, 2008.
- [15] E. LINDMAN, *Free-space boundary conditions for the time dependent wave equation*, Journal of Computational Physics, 18 (1975), pp. 66 – 78.
- [16] L. NANNEN, *Hardy-Raum Methoden zur numerischen Lösung von Streu- und Resonanzproblemen auf unbeschränkten Gebieten*, dissertation, Georg-August-Universität zu Göttingen, 2008.
- [17] L. NANNEN AND A. SCHÄDLE, *Hardy space infinite elements for Helmholtz-type problems with unbounded inhomogeneities*, Wave Motion, 48 (2011).
- [18] D. RUPRECHT, A. SCHÄDLE, F. SCHMIDT, AND L. ZSCHIEDRICH, *Transparent boundary conditions for time-dependent problems*, SIAM J. Sci. Comput., 30 (2008), pp. 2358–2385.
- [19] F. SCHMIDT, *Solution of Interior-Exterior Helmholtz-Type Problems Based on the Pole Condition Concept: Theory and Algorithms*, habilitation thesis, Freie Universität Berlin, Fachbereich Mathematik und Informatik, 2002.
- [20] F. SCHMIDT AND P. DEUFLHARD, *Discrete transparent boundary conditions for the numerical*

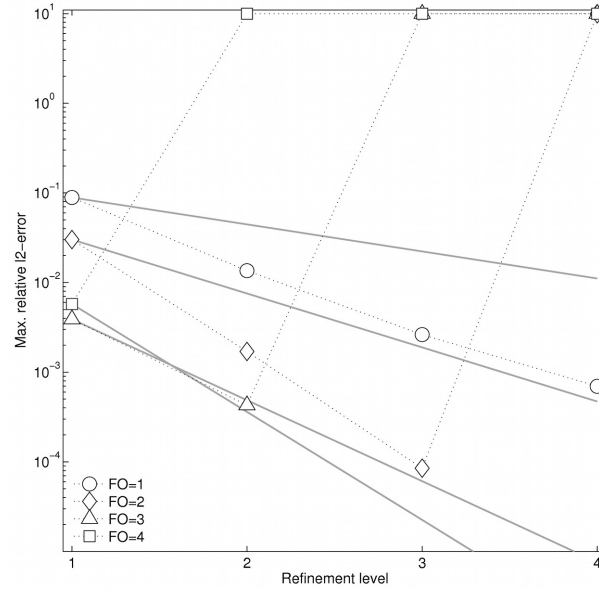


FIG. 4.9. Spatial order of convergence for the wave equation integrated until $T = 100$. Shown is the maximum l_2 -error over all generated outputs. The error is capped at 10^1 , so depicted error values of 10 correspond to unstable runs.

- solution of Fresnel's equation*, Comput. Math. Appl., 29 (1995), pp. 53–76.
- [21] F. SCHMIDT, T. HOHAGE, R. KLOSE, A. SCHÄDLE, AND L. ZSCHIEDRICH, *Pole condition: A numerical method for Helmholtz-type scattering problems with inhomogeneous exterior domain*, J. Comp. Appl. Math., 218 (2008), pp. 61–69.
 - [22] F. SCHMIDT AND D. YEVICK, *Discrete transparent boundary conditions for Schrödinger-type equations*, J. Comput. Phys., 134 (1997), pp. 96–107.
 - [23] S. TSYNKOV, *Numerical solution of problems on unbounded domains. A review*, Applied Numerical Mathematic, 27 (1998), pp. 465–532.
 - [24] L. ZSCHIEDRICH, *Transparent Boundary Conditions for Maxwell's Equations: Numerical Concepts beyond the PML Method*, dissertation, FB Mathematik, Freie Universität Berlin, 2009.
 - [25] L. ZSCHIEDRICH, R. KLOSE, A. SCHÄDLE, AND F. SCHMIDT, *A new finite element realization of the Perfectly Matched Layer Method for Helmholtz scattering problems on polygonal domains in 2D*, J. Comput Appl. Math., 188 (2006), pp. 12–32.

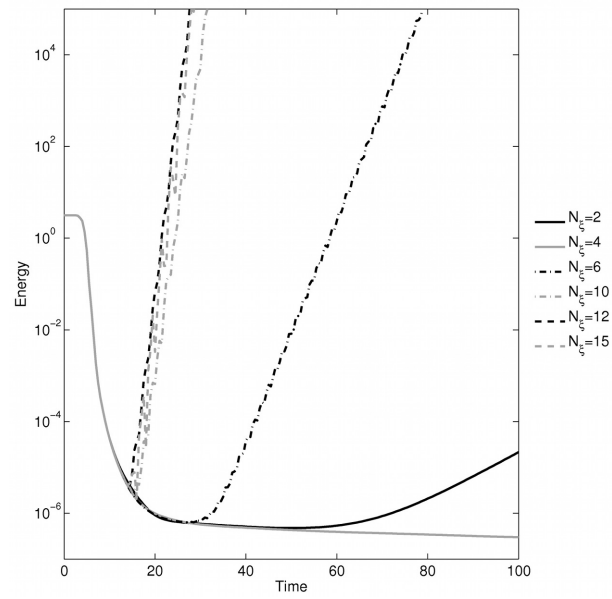


FIG. 4.10. Energy over time for the wave equation for different values of N_ξ . The refinement level of the mesh is two and the order of the used finite elements is four.